A SENSITIVITY ANALYSIS OF CFD TRANSITION MODELLING IN THE CONTEXT OF VORTEX ROLL-UP PREDICTION

RENS LIEBRAND[*], MAARTEN KLAPWIJK[†,‡], THOMAS LLOYD[⋆], GUILHERME VAZ[⋆], and RUI LOPES[‡,◇]

[*] Faculty of Aerospace Engineering
rensliebrand@gmail.com
[†] Faculty of Mechanical, Maritime and Material Engineering
Delft University of Technology
Mekelweg 5, 2628 CD Delft, The Netherlands

[‡] Maritime Research Institute Netherlands (MARIN) academy, [⋆] MARIN
Haagsteeg 2, 6708 PM Wageningen, The Netherlands

[◇] Instituto Superior Técnico
University of Lisbon
Av. Rovisco Pais 1, 1049-001 Lisbon, Portugal

Key words: Cavitating tip vortex noise, elliptical wing, transition modelling, ReFRESCO

Abstract. A sensitivity analysis of the transitional flow over a NACA66$_2$ − 415 foil and the elliptical Arndt wing is carried out. The SST turbulence model is complemented with the $\gamma - \tilde{R}e_{\theta_t}$ transition model to determine the effect of varying turbulence intensity and eddy-viscosity ratio on the integral quantities and transition locations. Local grid refinement at the transition location is used to improve convergence. The skin friction drag coefficient is found to be more sensitive to the inflow conditions for 5° angle of attack compared to 9°. The movement of the transition location on the suction side is found to be responsible for this. The transition model captures a laminar separation bubble at the pressure side for both angles of attack, causing the lift coefficient to drop slightly. 3D calculations for the Arndt wing with the same foil section show that applying a transition model can decrease the boundary layer thickness by a factor of three, which is expected to influence the viscous core radius and consequently the minimum pressure in the tip vortex.

1 INTRODUCTION

Motivated by increased awareness of the harmful environmental effects of underwater noise generated by ships, there is a need to better understand the noise-generation mechanisms. An important contributor to ship noise is propeller cavitation [1]. While the numerical prediction of developed sheet cavitation is relatively well-understood [2], knowledge regarding modelling aspects of the inception and dynamics of tip vortex cavitation is still insufficient to obtain reliable numerical results in relation to noise predictions.

A popular approach for studying cavitating vortices is to investigate a tip-loaded finite span lifting surface which induces a tip vortex while avoiding rotational motion. An often-used benchmark is the elliptical wing with NACA66$_2$ − 415 cross-section as introduced by Arndt et al [3]. Recent experimental

[4] and numerical studies [5, 6, 7] revealed the complexity of the cavitating vortex flow. Figure 1 provides a summary of the numerically as well as experimentally obtained lift coefficients (C_L) for an angle of attack (α) of 9° found in open literature. The spread in the values indicates the high uncertainties and lack of consensus regarding appropriate modelling for this test case.

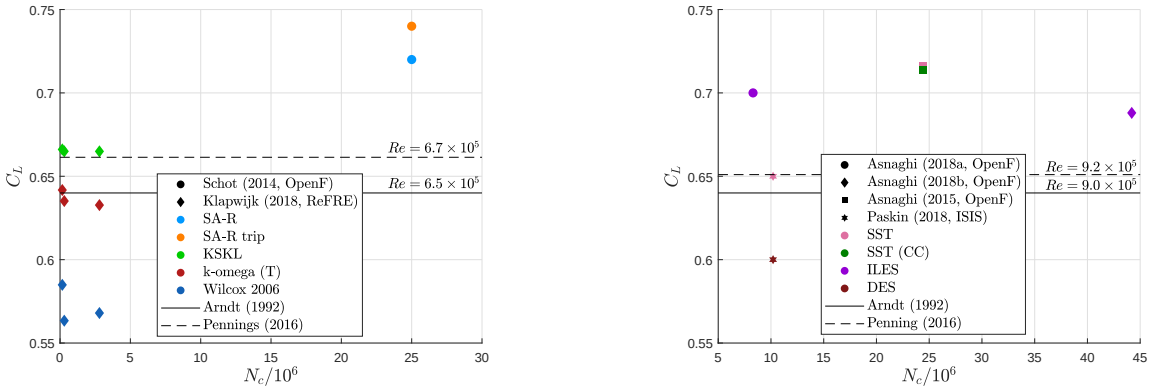

Figure 1: Published lift coefficient data versus number of grid cells (N_c) at $\alpha = 9°$, $Re = 6.8 \times 10^5$ (left) and $Re = 8.95 \times 10^5$ (right). The shape of the data points indicates the reference, the colour stands for the employed turbulence models, and the lines represent experimental results.

Most numerical studies assess the wing at 9° Angle of Attack (AoA) to avoid the presence of a Laminar Separation Bubble (LSB) [5]. Arndt et al [3] show a high dependency of the transition location on the suction side towards the AoA. Flow visualisation for an AoA of 10° at a Reynolds number (Re) of 5.3×10^5 shows natural transition occurring near the leading edge. This is probably due to the foil's geometry, which is designed to be a laminar foil (with a low adverse pressure gradient over the midsection of the foil) and therefore is not supposed to operate at such a high AoA. An AoA of 5° at the same Reynolds number shows laminar flow until $x/c \simeq 0.60$, after which it undergoes separation-induced transition [3]. Here x/c indicates the normalised stream-wise position from the leading edge, where c is the chord.

Although the lift coefficient is directly proportional to the circulation over the wing and thus the strength of the vortex, it does not provide a detailed insight into its structure. In CFD calculations, difficulties in the prediction of the transition location cause errors in the prediction of the Boundary Layer (BL) profile over the wing. Since the BL rolls up in the wake of a lifting surface, it is evident that the structure of the vortex is related to its characteristics. Maines and Arndt [8] observe that "*the vortex mainly interacts with the boundary layer on the suction side of the wing, boundary layer fluid is entrained in the vortex which affects the core radius*". This observation can be combined with the McCormick hypothesis resulting in the following proportionality,

$$\eta_v \sim \delta_s \sim Re_c^{-h}, \tag{1}$$

with η_v the viscous core radius, δ_s the BL thickness on the suction side, and $Re_c = \frac{U_\infty c}{\nu}$ the chord-based Reynolds number. In this equation U_∞ is the freestream velocity, and ν the kinematic viscosity. The constant h is typically about 0.2 for a turbulent BL and 0.4 for a transitional BL [9].

The flow characteristics within the vortex core play a crucial role in the cavitation inception process as well as the dynamics of the cavity. Bosschers [1] derived a two-dimensional analytical expression for the velocity and pressure distributions within a cavitating vortex. The derivation is based on the Lamb-Oseen vortex which is supplemented by jump relations for the mass transfer and shear stress as boundary

conditions at the vapour-liquid interface. The pressure is supposed to be at its minimum (p_{min}) in the centre of the vortex core ($\eta = 0$). This yields the relation,

$$p(\eta = 0) - p_\infty = p_{min} - p_\infty = -\frac{\rho \Gamma_\infty^2}{(2\pi\eta_v)^2}\zeta \ln(2)\,, \tag{2}$$

where the pressure is denoted by p, the freestream pressure by p_∞, and the freestream circulation of the vortex by Γ_∞. The latter is related to the circulation over the wing (Γ_0) through the roll-up process. The constant $\zeta = 1.2564$ is introduced to ensure that the azimuthal velocity is maximum at the viscous core radius.

When employing a transition model, the resulting BL thickness is expected to be predicted more accurately. In most applications, a transition model delays the mixing properties of the BL which yields a laminar profile over a longer distance. This means that the resulting BL is thinner and thus the viscous core length smaller, according to Equation 1. Following Equation 2, this results in a lower minimum pressure and therefore more cavitation. While in prior research [5, 6] the under-predicted vortex cavity length is explained by (i) over-prediction of the eddy-viscosity in the vortex core and (ii) numerical diffusion, it could be that the assumption of a fully turbulent BL also contributes.

Prior to considering the vortex itself to test this hypothesis, it is important to understand the transitional behaviour of the flow over the foil section under different flow conditions. To this end, a 2D sensitivity analysis of the foil at half-span to the turbulent inflow conditions is performed. The effect on the lift coefficient C_l and friction drag coefficient C_{d_f} is investigated. To draw more general conclusions concerning transition, the 2D simulations were carried out for two AoA: 5° and 9°. Based on these findings, a set of 3D calculations is performed to investigate the effect on the BL itself.

2 NUMERICAL MODELS

Reynolds-Averaged Navier Stokes (RANS) calculations are performed which are by definition not able to capture transitional flows [10]. The 2003 version of the SST [11] turbulence model was complemented with the $\gamma - \tilde{Re}_{\theta_t}$ model [12] to model this process. Downstream of the stagnation point, a turbulent BL starts developing due to the production term P_k in the transport equation for turbulent kinetic energy k.

The $\gamma - \tilde{Re}_{\theta_t}$ model solves a transport equation for the intermittency γ which ranges from 0 (laminar flow) to 1 (turbulent flow). The intermittency is used to adapt the production and destruction term in the k-transport equation,

$$\tilde{P}_k = \gamma_{eff} P_k; \qquad \tilde{D}_k = \min[\max(\gamma_{eff}, 0.1), 1.0] D_k\,, \tag{3}$$

where $\gamma_{eff} = \max(\gamma, \gamma_{sep})$. Here γ_{sep} is a modification to the intermittency for predicting separation induced transition. Using the intermittency to adapt the production and dissipation terms instead of modifying the eddy-viscosity increases the robustness of the model. In this way, γ does not enter the momentum equation directly and therefore does not have to be linearised (which is difficult because of the empirical relations in the source term shown later).

The transport equation for the intermittency reads:

$$\frac{\partial \gamma}{\partial t} + \frac{\partial (u_j \gamma)}{\partial x_j} = P_\gamma - E_\gamma + \frac{\partial}{\partial x_j}\left[\left(\nu + \frac{\nu_t}{\sigma_f}\right)\frac{\partial \gamma}{\partial x_j}\right], \tag{4}$$

$$\text{with} \qquad P_\gamma = F_{length} c_{a1} S \left[\gamma F_{onset}\right]^{0.5} (1 - c_{e1}\gamma)\,.$$

At the start of the BL, $\gamma = 0$ indicates a completely laminar flow. When the BL develops, the intermittency is mainly increased by the production P_γ. This term acts as a source and is designed to be 0

upstream of the transition point and to be active when transition starts, achieved by the limiter F_{onset}. Mathematically the model triggers transition when the vorticity based Reynolds number (Re_V) exceeds the onset criterion. The onset criterion is determined by the *local* transition Reynolds number ($\tilde{Re}_{\theta_t}$) according to the following proportionality,

$$F_{onset} \overset{\text{I. limiter}}{\sim} F_{onset2} \overset{\text{II. limiter}}{\sim} F_{onset1} \overset{\text{III. expression}}{\sim} Re_{\theta_c} \overset{\text{IV. empirical relation}}{\sim} \tilde{Re}_{\theta_t} \overset{\text{V. diffusion in TE}}{\sim} Re_{\theta_t}. \tag{5}$$

The description of proportionality I-IV can be found in the original paper [12]. The fifth relation is incorporated in the second transport equation:

$$\frac{\partial \tilde{Re}_{\theta t}}{\partial t} + \frac{\partial \left(u_j \tilde{Re}_{\theta t}\right)}{\partial x_j} = P_{\theta t} + \frac{\partial}{\partial x_j}\left[\sigma_{\theta t}\left(\nu + \nu_t\right)\frac{\partial \tilde{Re}_{\theta t}}{\partial x_j}\right], \tag{6}$$

$$\text{with} \qquad P_{\theta t} = \frac{c_{\theta_t}}{t}(Re_{\theta t} - \tilde{Re}_{\theta t})(1.0 - F_{\theta t}). \tag{7}$$

Information from the freestream is passed into the BL by means of the diffusion term. In order to match the local and global variable in the freestream, the production term is employed. The blending factor F_{θ_t} is responsible for deactivating the production inside the BL and activating the term in the freestream. In this blending factor a function F_{wake} ensures that the production term is *not* active in the wake regions.

The behaviour of the model is known to be sensitive to the turbulent inflow quantities, turbulent intensity I and eddy-viscosity ratio $\frac{\nu_t}{\nu}$ [10, 12]. By shifting the transition location, through varying the turbulent inflow conditions, the hypothesis stated in Section 1 can be tested.

3 COMPUTATIONAL SETUP

The computational domain is based on to the cavitation tunnel at Delft University of Technology. The Arndt wing is an elliptical planform with a $NACA66_2 - 415$ cross-section over its entire span. In the 2D computations, the wing at half-span ($z/b = 0.5$) is considered. This spanwise location is chosen since least interaction with the tip flow and the side wall is expected there. The chord length at this location is $c = 109.2\ mm$. The domain extends $6c$ up- and $13c$ downstream of the foil's leading edge. The distance between the leading edge and the top and bottom walls is $1.35c$. Most available 3D reference data is for a *root* chord-based Reynolds number of 8.95×10^5 as shown in Figure 1, corresponding to a Reynolds number at half-span (for 2D computations) of 7.76×10^5. Using $\nu = 1.002 \times 10^{-6}\ m^2/s$, this yields an inflow velocity of $0.7783\ m/s$. Both $\alpha = 5^\circ$ and $\alpha = 9^\circ$ were simulated. The turbulence intensity and the eddy-viscosity ratio were varied between $I = [1,2,3]\%$ and $\frac{\nu_t}{\nu} = [1,2,3]$. The turbulent quantities are frozen until $0.1c$ upstream of the leading edge of the foil to control the decay in the domain.

A set of four geometrically similar O-grids with a refinement factor of 1.6 between coarsest and finest grid was generated for each AoA. Table 1 displays the details of the grids.

Simulations were performed using ReFRESCO (`www.refresco.org`), a community based open-usage/open-source CFD code for the Maritime World. It solves multiphase (unsteady) incompressible viscous flows using the Navier-Stokes equations, complemented with turbulence models, cavitation models and volume-fraction transport equations for different phases. The equations are discretised using a finite-volume approach with cell-centred collocated variables, in strong-conservation form, and a pressure-correction equation based on the SIMPLE algorithm is used to ensure mass conservation. The implementation of the $\gamma - \tilde{Re}_{\theta_t}$ model in the solver was tested by [13]. For the convective flux discretisation, the second-order accurate Quadratic Upstream Interpolation for Convective Kinematics (QUICK)

Table 1: 2D grid specifications for $\alpha = 5^\circ$ (left) and $\alpha = 9^\circ$ (right). Normal x_n^+ and tangential x_t^+ wall coordinates are averaged over the surface and obtained by the *SST* simulation. N_s indicates the number of surface cells, N_c the total number of grid cells, and h/h_i the refinement ratio.

N_s	$N_c/10^5$	h/h_i	$\overline{x_n^+} \times 10^2$	$\overline{x_t^+}/10^2$
600	1.00	1.60	9.23	1.41
720	1.44	1.33	7.64	1.17
840	1.96	1.14	6.51	1.01
960	2.56	1.00	5.68	0.88

N_s	$N_c/10^5$	h/h_i	$\overline{x_n^+} \times 10^2$	$\overline{x_t^+}/10^2$
600	1.00	1.60	9.81	1.36
720	1.44	1.33	8.11	1.14
840	1.96	1.14	6.92	0.97
960	2.56	1.00	6.03	0.85

scheme is employed for the momentum and turbulence equations. A First-Order accurate Upwind (FOU) scheme is used for the transition equations for robustness reasons as elaborated on in Section 5.1. The discretisation of all diffusive terms is second order accurate. Computations are performed steady state since no large separation or vortex shedding was observed by experimentalists [3].

4 ERROR ANALYSIS

In CFD one can distinguish between iterative, discretisation, input, round-off and, for unsteady calculations, statistical errors. The transition model is known be to sensitive to input (parameter) uncertainties, however the assessment of this is not part of this research. Round-off errors can be assumed to be negligible in practical applications [14]. In the 2D sensitivity analysis, the iterative and discretisation error were evaluated.

4.1 Iterative error

To ensure effective use of computational resources, a trade-off between computational costs and iterative error was made. For each AoA, six calculations with different convergence criteria for the maximum residual (L_∞) were performed. The residuals for the transition equations are excluded from these criteria since it was not possible to reach $L_\infty = 10^{-7}$ and $L_\infty = 10^{-8}$ using the FOU scheme for the convective fluxes of γ and $\tilde{Re}_{\theta_t}$. Figure 2 displays the most relevant quantity for transition, C_{df}, versus the convergence criteria. The right axis shows the computational costs to reach the specified L_∞. Making a trade-off between computational costs and iterative accuracy, a convergence criterion of $(L_\infty)_{\notin \gamma,\, \tilde{Re}_{\theta_t}} = 10^{-5}$ is considered to be sufficient for both cases. At that level, the iterative errors relative to the 10^{-8} simulation are 0.40% and 0.31% for $\alpha = 5^\circ$ and $\alpha = 9^\circ$ respectively. In order to reduce this error to 0.14% and 0.07% at $(L_\infty)_{\notin \gamma,\, \tilde{Re}_{\theta_t}} = 10^{-6}$, the computational costs increase by 132% and 111%.

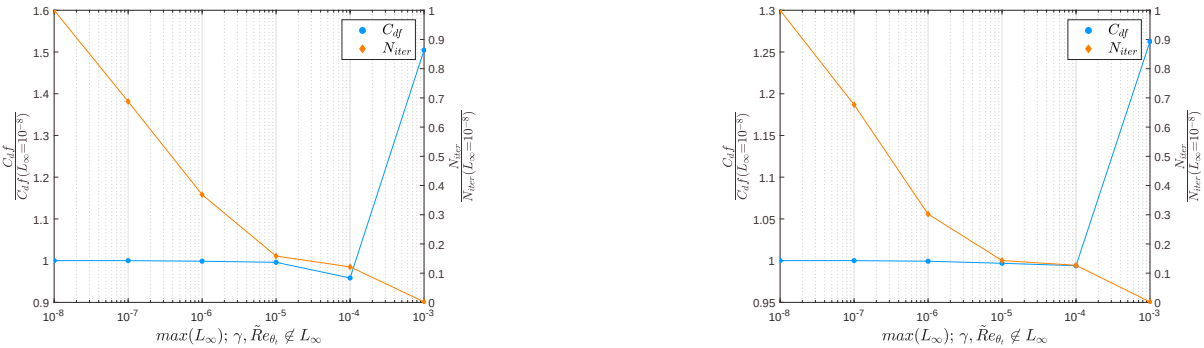

Figure 2: Iterative error analysis for $N_s = 960$ grid, showing the trade-off between numerical accuracy and computational cost for $\alpha = 5^\circ$ (left) and $\alpha = 9^\circ$ (right).

4.2 Discretisation error

The discretisation error was assessed based on the procedure of Eça and Hoekstra [15]. The method relies on (truncated) power series expansions. The basic equation to determine the discretisation error ε for the variable ϕ reads,

$$\varepsilon \simeq \phi_i - \phi_0 = \beta h_i^q \,, \tag{8}$$

where ϕ_i is any local or integrated flow quantity, ϕ_0 an estimate of the exact solution, β a constant to be determined, h_i the typical cell size and q the observed order of grid convergence. To determine ϕ_0, β, and q, a set of four geometrically similar structured grids is used, as presented in Table 1. Flux limiters, damping functions and switches in the turbulence model result in noise in the CFD output. This sometimes yields the proposed estimation in Equation 8 to be impossible or unreliable. In that case, either a linear ($q = 1$), quadratic ($q = 2$), or a combination of both ($\beta_1 h_i + \beta_2 h_i^2$) is used.

The resulting uncertainty U_ϕ is determined according to the Grid Convergence Index procedure [14],

$$U_\phi(\phi_i) = F_s \varepsilon(\phi) + \sigma + |\phi_i - \phi_{i_{fit}}| \,, \tag{9}$$

where the safety factor F_s is set as 1.25 or 3 depending on the quality of the fit, to obtain a 95% confidence interval for U_ϕ. The uncertainties of the integral values (C_l and C_{d_f}) were determined using this approach. These results are visualised by the error bars in Figure 6.

5 RESULTS

5.1 Iterative convergence

A well-known problem of the $\gamma - \tilde{Re}_{\theta_t}$ model is its convergence behaviour, see e.g. [16]. If a FOU scheme for the discretisation of the convection of the transition variables is employed, the simulations converge to the residual criterion ($L_\infty = 10^{-5}$). However, when using the QUICK scheme in all equations the calculation stagnate. Although the residuals are not converged, the forces are observed to be constant over the stagnated part ($N_{iter} > 1.2 \times 10^4$). N_{iter} is the number of iterative loops used to solve the non-linearity in the Navier-Stokes equations.

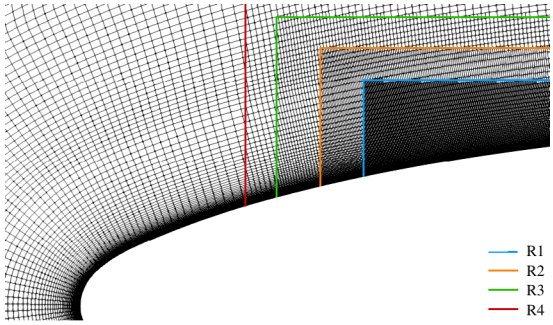

Figure 3: Grid of the suction side at the leading edge, $N_s = 600$. Colours indicate refinements.

The stagnating behaviour is related to the transition location continuously switching between two streamwise cells. If the location moves to the neighbouring cell, the flow-field adapts itself accordingly whereafter the transition location moves back to the original location again. This can be explained by the fact that the γ-production is triggered by the limiter $F_{onset} = \max(F_{onset2} - F_{onset3}, 0)$. In the γ-production term, the magnitude of F_{length} is typically large whereby the production increases drastically when F_{onset2} exceeds F_{onset3}. F_{onset3} is relatively constant throughout the simulation since it only depends on k and the specific dissipation rate (ω). The main term responsible for triggering the onset of production is thus F_{onset2}. This term is implicitly related to the strain rate (S_{ij}) in the flow by $F_{onset2} \sim F_{onset1} \sim Re_V \sim S_{ij}$, which causes the observed behaviour. When production of γ starts, P_k, and thus k and ν_t, increase. The resulting higher eddy-viscosity smooths the solution which reduces the magnitude of the gradients. This results in a lower strain rate causing $Re_v \sim F_{onset1} \sim F_{onset2}$ to drop. If this drop is sufficient, the magnitude of

F_{onset2} ends up lower than F_{onset3} whereby the limiter cancels the production term again. Although F_{onset3} is introduced to avoid this sort of behaviour [12], it fails to do so in this case.

This reasoning is tested by means of local grid refinement (h-refinement) at the transition location (x_{tr}). The transition location is defined as the point where the derivative of the skin friction changes from negative to positive. If the grid is sufficiently fine in the stream-wise direction (x_t^+), the iterative stagnating behaviour should be absent. The four different refinement levels applied at the suction side (R1-4) are shown in Figure 3. All refinement levels are applied on the baseline grid with $N_s = 600$.

The largest residuals in the original simulation were located at the point of transition on the suction side. *Only* refining at that location does not yield convergence but shifts the maximum residual towards the transition location at the pressure side. Convergence is obtained when the grid around both transition locations is sufficiently refined while controlling the grid diffusion. Table 2 presents all relevant quantities of the refined grids.

Table 2: Grid refinement on the suction side (left) and pressure side (right). Values for x_t^+ at the transition location and x_{tr} given for the corresponding side. x_t^+ on opposite side was 9.1 for simulations *a*-*d*, and 11.8 for simulations *e*-*h*.

Sim.	$N_c/10^5$	x_t^+	$\frac{C_l}{(C_l)_{d,h}}$	$\frac{C_{df}}{(C_{df})_{d,h}}$	$\frac{x_{tr}}{(x_{tr})_{d,h}}$
a	1.35	99.1	1.0012	0.9950	1.0308
b	1.43	47.3	1.0006	0.9973	1.0301
c	1.58	23.7	1.0005	0.9989	1.0240
d	1.89	11.8	1.0000	1.0000	1.0000

Sim.	$N_c/10^5$	x_t^+	$\frac{C_l}{(C_l)_{d,h}}$	$\frac{C_{df}}{(C_{df})_{d,h}}$	$\frac{x_{tr}}{(x_{tr})_{d,h}}$
e	1.59	71.8	1.0008	1.0006	0.9997
f	1.63	36.2	1.0003	0.9986	1.0006
g	1.72	18.2	1.0003	0.9987	1.0002
h	1.89	9.1	1.0000	1.0000	1.0000

When using a QUICK scheme for the transition variables without local grid refinement, the computation typically stagnates with the γ-residual being the largest as shown in Figure 4. Figure 5 displays the residuals of the γ-equation for all refinement levels. In order to obtain convergence, a maximum x_t^+ of ~ 24 and ~ 36 is required on the suction and pressure side respectively. These values are expected to be case specific. Local grid refinement yields small discontinuities in the derivative of the skin friction distribution.

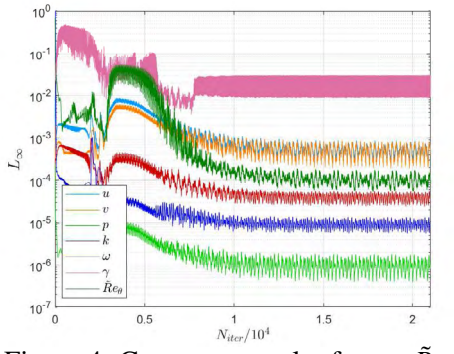

Figure 4: Convergence plot for $\gamma - \tilde{Re}_{\theta_t}$ simulation, $\alpha = 5^\circ$ and $N_s = 600$. QUICK is employed for *all* flux discretisations.

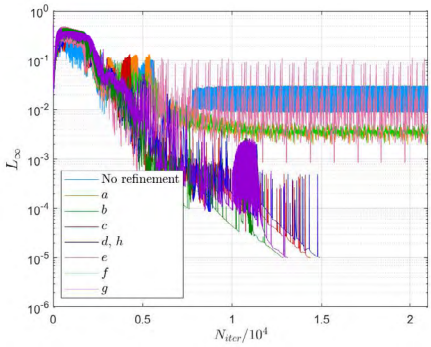

Figure 5: Convergence of γ-residual for all simulations present in Table 2. Stagnated QUICK simulation is also included.

5.2 Sensitivity to inflow conditions

A final simulation was performed using the minimum required x_t^+ values. This converged QUICK simulation only differs 0.65% for C_l, 0.25% for C_{df}, and 0.96% for x_{tr} with respect to a converged FOU simulation without refinement. Considering the increase of computations costs and effort of local grid refinement to obtain convergence if a QUICK scheme is employed in all equations, it was decided to use the FOU settings for the transition variables in this sensitivity analysis.

Figure 6 presents the sensitivity of the integral values towards the inflow conditions. The pure *SST* result for $I = 1\%$ and $\frac{\nu_t}{\nu} = 1$ is also given, in red. All results are normalised by the $\gamma - \tilde{Re}_{\theta_t}$ simulation with $I = 1\%$ and $\frac{\nu_t}{\nu} = 1$. Transition predominantly affects the C_{df} since it changes the shape of the BL and thus the velocity derivative at the wall, $C_{df} \sim \tau_w \equiv \mu \left(\frac{\partial u}{\partial y}\right)_{y=0}$. Furthermore, the transition model could influence the pressure distribution and thus the lift coefficient by its ability to capture an LSB or predicting laminar and turbulent separation more accurately.

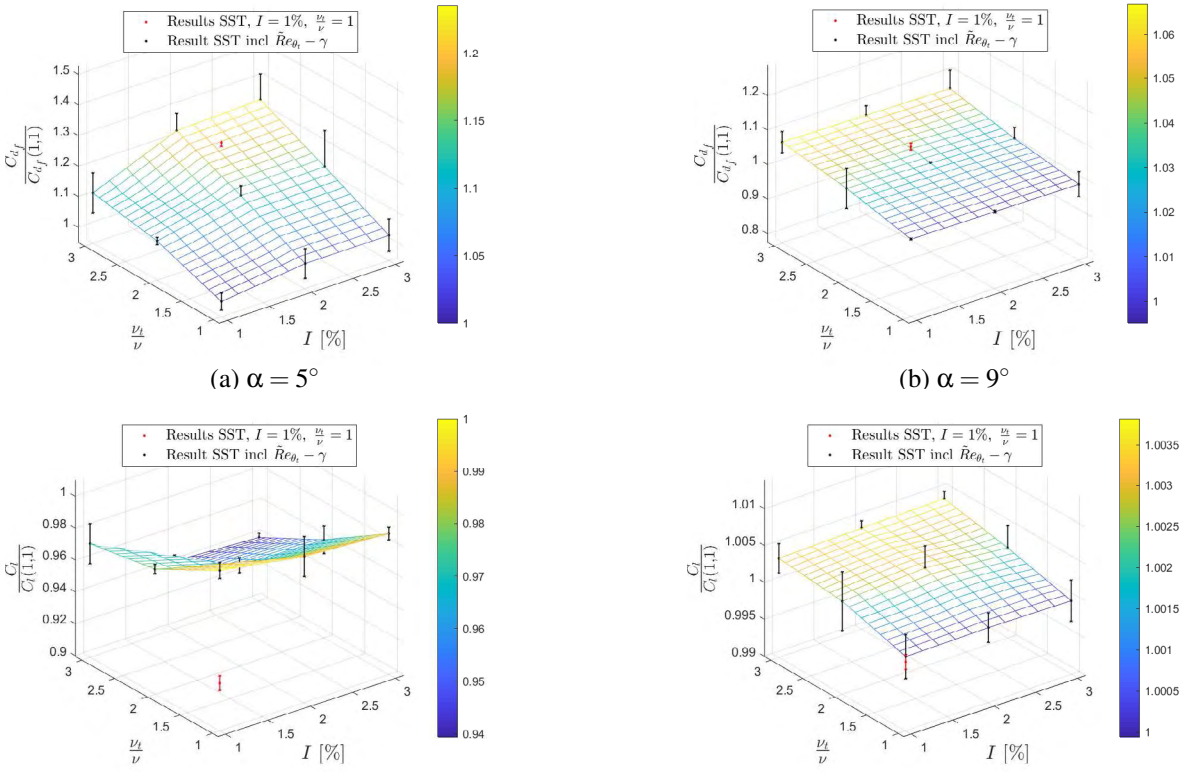

(a) $\alpha = 5°$ (b) $\alpha = 9°$

(c) $\alpha = 5°$ (d) $\alpha = 9°$

Figure 6: Sensitivity of the integral quantities to the turbulent inflow conditions for both AoA, using a grid with $N_s = 960$. The error bars indicate the discretisation uncertainty.

The skin friction for both AoA is significantly affected by changing the inflow conditions; it increases about 25% for $\alpha = 5°$ and 6% for $\alpha = 9°$. This is due to the up- or downstream movement of the transition location on the suction and pressure side of the foil. It can be observed that C_{df} for $\alpha = 9°$ is less sensitive which is due to the high leading edge curvature at a higher AoA, forcing transition independently of the turbulent state of the inflow. This is confirmed by the skin friction distributions shown in Figure 7 where the high curvature of the leading edge causes the magnitude of the skin friction to be large for $x/c < 0.1$

which triggers transition. For $\alpha = 5°$, transition on the suction side occurs at $x/c \simeq 0.2$ resulting in a completely different distribution.

Figure 7: Skin friction (left) and pressure (right) distributions for both AoA. Both SST and $\gamma - \tilde{R}e_{\theta_t}$ ($[I, \frac{\nu_t}{\nu}] = 1$) results are shown.

As expected, the lift coefficient is less sensitive to the turbulent inflow quantities. For $\alpha = 5°$, the change in lift coefficient is at maximum 6%, for $\alpha = 9°$ this reduces to only 0.4%. The fact that the 5° AoA case is influenced more is due to the shift in transition location on the suction side. The location where the flow undergoes transition determines its sensitivity to turbulent separation at the aft of the foil. This can be recognised in the friction and pressure distributions in Figure 7 at the location where C_f is smaller than zero at the trailing edge for the $\alpha = 5°$, $\gamma - \tilde{R}e_{\theta_t}$ simulation. For both AoA, the lift coefficients predicted by the pure SST simulations are lower compared to the $\gamma - \tilde{R}e_{\theta_t}$ simulations. The LSB on the *pressure* side, captured by the $\gamma - \tilde{R}e_{\theta_t}$ model, is partly responsible for this. For both AoA, an LSB is present at $x/c \approx 0.75$ causing a reduced pressure and therefore a slightly lower lift coefficient.

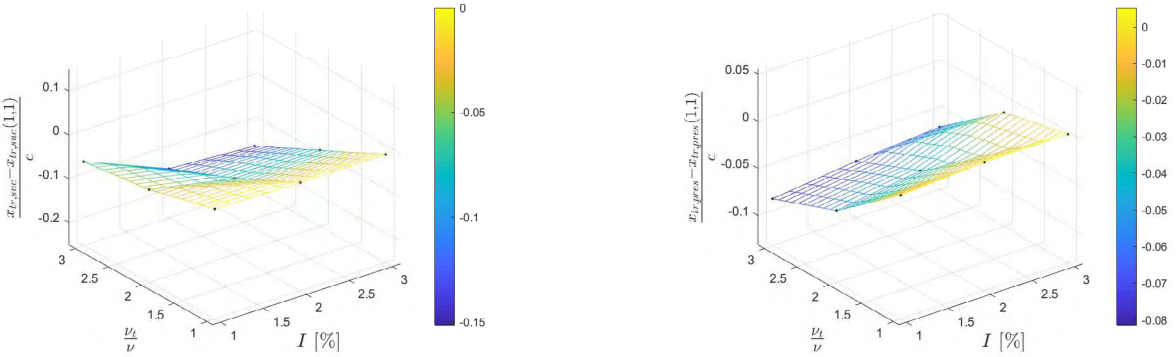

(a) $\alpha = 5°$ (b) $\alpha = 9°$

Figure 8: Sensitivity of the transition locations towards the turbulent inflow conditions for both angles of attack on grid with $N_s = 960$.

To further clarify the sensitivities of the integral quantities, Figure 8 presents the sensitivity of the transition locations. All results are reported with respect to the transition location for $I = 1\%$ and $\frac{\nu_t}{\nu} = 1$. Only the sensitivity of the transition location on the suction side for $\alpha = 5°$ and the transition location on the pressure side for $\alpha = 9°$ are shown. The other results are almost independent of the inflow conditions ($< 4\%$). The transition location on the suction side for $\alpha = 5°$ moves 15% upstream if both quantities are tripled. This is intuitive since more energetic turbulence upstream should yield earlier transition. In the model, this is incorporated by the empirical relation between I and the *global* Re_{θ_t}. It is interesting to note that the results are insensitive when *only* the turbulence intensity is varied. This is due to the

decay of turbulence in the domain. Increasing the eddy-viscosity ratio accordingly avoids this since a higher $\frac{\nu_t}{\nu}$ reduces the damping. For 9° AoA, the transition location on the suction side is barely changed, a maximum shift of 0.3% is observed.

Transition on the pressure side is triggered at almost the same location for both cases. This location varies more for the 9° AoA case (maximum of ∼8%) than for the 5° AoA case (maximum of ∼4%). For both cases, it moves upstream for the reasons previously given. This causes the BL to become turbulent earlier which explains the increased C_{df} as discussed earlier.

5.3 3D wing calculations

Based on the findings in the previous section, 3D calculations were performed. The ultimate goal is to study the effect of transition modelling on the vortex structure itself; here some preliminary work towards this objective is presented. In Section 1, a hypothesis was stated which resulted in, $p_{min} \overset{\text{Eq. 2}}{\sim} 1/\eta_v^2 \overset{\text{Eq. 1}}{\sim} 1/\delta_s^2$. While this relationship between δ_s, η_v, and p_{min} will be examined in a future study, the current work focuses on the BL thickness.

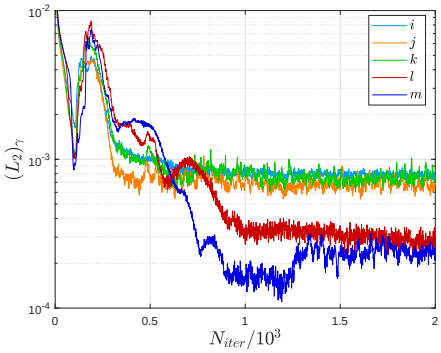

Figure 9: Average γ residuals for locally refined 3D grids. Foil at 5° AoA with $[I, \frac{\nu_t}{\nu} = 1]$.

Sim.	$N_c/10^6$	$\overline{x_t^+}$	$\overline{x_s^+}$	$\frac{C_L}{(C_L)_m}$	$\frac{C_{Df}}{(C_{Df})_m}$
i	2.69	289	273	0.9978	0.9852
j	2.79	178	198	0.9992	0.9870
k	3.13	94.9	110	0.9995	0.9956
l	4.44	50.6	63.2	1.0003	0.9920
m	9.51	26.7	33.3	1.0000	1.0000

Table 3: 3D simulation details of local grid refinement study. Wall-coordinates at pressure side are shown, they are averaged values at the transition location over the entire span.

Calculations are performed on a structured grid with $N_c = 2.61 \times 10^6$. Vortex refinement according to the recommendations of Asnaghi [6] and wake refinement to capture the gradients in the roll-up process more accurately are applied. The average wall coordinates over the surface are 0.147, 343, and 698 for x_n^+, x_t^+ and x_s^+ respectively. Here x_s^+ indicates the non-dimensional wall unit in spanwise direction.

The same approach as for the 2D results is taken to improve convergence. The grid details are shown in Table 3, refinement is applied in the streamwise and spanwise direction until the requirement of ~ 36 non-dimensional wall units is reached. The residuals for the γ-equation are again observed to be the highest, and they are located at the transition location on the pressure side. Locally refining the grid at the pressure *and* suction sides based on the requirements set in Section 5.1 reduced the average (L_2) residual by a factor of four, as can be seen in Figure 9 (the graph only shows the first $2 \cdot 10^3$ iterations while a total of $2 \cdot 10^4$ iterative loops is performed). However, still small areas with the same value for the maximum residuals remain, i.e. L_∞ remains unaffected. This yields stagnation of the computations even though a FOU scheme is used for the turbulence *and* transition equations. This may be due to the omission of cross-flow instabilities in the $\gamma - \tilde{Re}_{\theta_t}$ model and/or the robustness of the model [12].

Further refinement would result in too large grids for a sensitivity analysis, and was therefore not pursued. Forces were observed to be constant over the iterations in the stagnated region. As shown in Table 3, the lift and skin friction drag coefficients only differ with 0.2% and 1.5% respectively. Although

the computations stagnate, the high residuals were found to occur very locally, at the transition location on the pressure side. Therefore the flow field on the side of interest (suction side) is not expected to be affected. Furthermore, the maximum and root mean square residuals for all other variables are at least one order of magnitude lower compared to the residuals of the γ equation. For all these reasons it was decided to perform the 3D calculations on the original grid *without* refinement at the transition locations.

Figure 10 visualises the flow over the suction side of the wing. On both sides, a LSB is present. The flow is laminar upstream of the LSB, following which separation induced transition causes the flow to become turbulent. The shape factor, which is defined as the displacement thickness over the momentum thickness, provides more insight in the flow. This number reflects the 'fullness' of the profile and is therefore directly related to the state of the BL. Figure 11 shows that transition for the $[I, \frac{\nu_t}{\nu}] = 1$ and $[I, \frac{\nu_t}{\nu}] = 0.5$ cases occurs at $x/c \approx 0.6$ as H reduces from a laminar value (2.6) towards the corresponding value for a turbulent BL (1.4). The fact that $H_{x/c=0.3} > 2.6$ is due to the adverse pressure gradient at that location. H drops below 2.6 between $x/c \simeq 0.3$ and 0.6 due to the favourable pressure gradient. BL details for $x/c > 0.8$ are excluded since turbulent flow separation results in an inaccurate estimation of H.

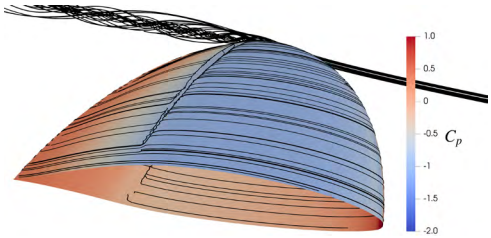

Figure 10: Flow (from right to left) at $\alpha = 5°$. Limiting streamlines and pressure coefficient is visualised on the surface.

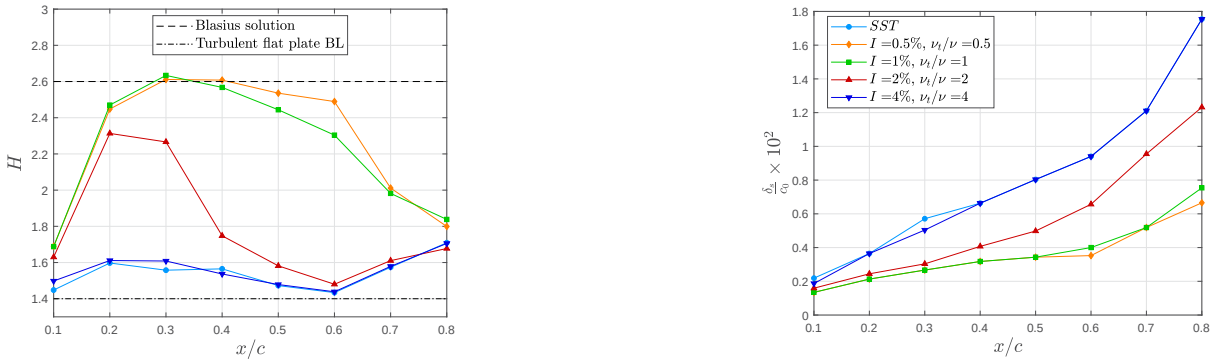

Figure 11: BL characteristics on the suction side over the chord at half-span ($z/b = 0.5$), shape factor (left) and BL thickness (right).

Figure 11 also shows the BL thickness on the suction side which is defined as the point where the magnitude of the velocity is less than 99% of the freestream velocity at that location, i.e. $|U| < 0.99|U_f|$. It can be seen that the δ_s for the *SST* and $[I, \frac{\nu_t}{\nu}] = 4.0$ case almost collapse. This is because for both cases transition occurs near the leading edge. The turbulence quantities are simultaneously decreased to a value of 2, 1 and 0.5. By doing so, transition is delayed which results in a BL almost three times thinner compared to the *SST* result at $x/c = 0.8$. This confirms the first part of the hypothesis: by varying the turbulent inflow conditions, the $\gamma - \tilde{Re}_{\theta_t}$ model changes the BL thickness at the suction side for $\alpha = 5°$ significantly. This knowledge can now be used to test the effect of transition modelling on the vortex core itself.

6 CONCLUSIONS AND RECOMMENDATIONS

In this study, the effect of modelling transition on the wing's BL was investigated as a first step towards confirming the hypothesis that links the BL flow and the pressure inside the vortex core. Local

grid refinement around the transition location was found to improve convergence when using the QUICK scheme for the convective flux discretisation in the transport equations of γ and $\tilde{Re}_{\theta_t}$. Results for C_l, C_{df} and x_{tr} obtained using the QUICK scheme and the FOU scheme are found to be within 1%.

It was observed that C_{df} is much more sensitive to the turbulent inflow conditions for $\alpha = 5^\circ$ than $\alpha = 9^\circ$. The lift coefficient is found to be relatively constant for both AoA. Accounting for transition results in an LSB on the pressure side for both AoA. Furthermore, at $\alpha = 5^\circ$, the sensitivity of the transition location on the suction side to the turbulent inflow conditions influences (turbulent) flow separation at the aft of the foil. Prescribing $I > 2\%$ in combination with $\frac{\nu_t}{\nu} > 2$ causes turbulent separation whereby the lift and thus the circulation drop by 6%.

3D calculations showed that δ_s at $x/c = 0.8$ decreases with a factor three when employing the $\gamma - \tilde{Re}_{\theta_t}$ model. Future work will focus on further evaluation of the hypothesis that this decrease in BL thickness decreases the minimum pressure in the vortex. In the light of this study, it is noted that since transitional effects are not controlled nor quantified in the (experimental) studies presented in Figure 1, it is expected that one should consider the results of these measurements for different AoA with care.

7 ACKNOWLEDGEMENTS

R. Liebrand would like to thank Dr M. Gerritsma and Dr A. van Zuijlen from the faculty of Aerospace Engineering of Delft University of Technology for their support and guidance during his MSc. thesis, part of which is reported in this paper. R. Lopes acknowledges the financial support provided by Fundação para a Ciência e Tecnologia through the Bolsas de Doutoramento and Pós-Doutoramento 2016 program.

REFERENCES

[1] Bosschers, J. (2018). *Propeller tip-vortex cavitation and its broadband noise*. PhD thesis, The Netherlands: University of Twente.

[2] Foeth, E.-J. (2008). *The structure of three-dimensional sheet cavitation*. PhD thesis, The Netherlands: Delft University of Technology.

[3] Arndt, R., Arakeri, V., and Higuchi, H. (1991). Some observations of tip-vortex cavitation. *Journal of fluid mechanics*, 229:269–289.

[4] Pennings, P. (2016). *Dynamics of vortex cavitation*. PhD thesis, The Netherlands: Delft University of Technology.

[5] Schot, J. (2014). *Numerical study of vortex cavitation on the elliptical Arndt foil*. Master's thesis, The Netherlands: Delft University of Technology.

[6] Asnaghi, A. (2018). *Computational modelling for cavitation and tip vortex flows*. PhD thesis, Sweden: Chalmers University of Technology.

[7] Paskin, L. (2018). *A numerical assessment of turbulence modelling in tip vortex flows at cavitating conditions*. Master's thesis, France: Ecole Centrale de Nantes.

[8] Maines, B. H. and Arndt, R. (1997b). Tip vortex formation and cavitation. *Journal of fluids engineering*, 199(2):413-419.

[9] McCormick, B. (1962). On cavitation produced by a vortex trailing from a lifting surface. *Journal of Basic Engineering, 84(3):369–378*.

[10] Lopes, R., Eça, L., and Vaz, G. (2018). Assessment of RANS transition models. *Proceedings of the 21st Numerical Towing Tank Symposium (NuTTS'18), Cortina, Italy*.

[11] Menter, F. R., Kuntz, M., and Langtry, R. (2003). Ten years of industrial experience with the SST turbulence model. *Turbulence, heat and mass transfer*, 4(1):625–632.

[12] Langtry, R. B. (2006). *A correlation-based transition model using local variables for unstructured parallelized CFD codes*. PhD thesis, Germany: Universität Stuttgart.

[13] Eça, L., Lopes, R., Vaz, G., Baltazar, J., and Rijpkema, D. (2016). Validation exercises of mathematical models for the prediction of transitional flows. *31st Symposium on Naval Hydrodynamics, 11th-16th September, Berkeley.*

[14] Roache, P.J. (2009). *Fundamentals of Verification and Validation*, Hermosa Publishers. Albuquerque, New Mexico.

[15] Eça, L. and Hoekstra, M. (2014). A procedure for the estimation of the numerical uncertainty of CFD calculations based on grid refinement studies. *Journal of Computational Physics*, 262:104–130.

[16] Baltazar, J., Rijpkema, D., and Falcão de Campos, J.A.C. (2017). On the use of the $\gamma - \tilde{Re}_\theta$ transition model for the prediction of the propeller performance at model-scale. *5th international symposium on marine propulsors, June, Finland.*